Published in final edited form as:

IEEE Trans Biomed Eng. 2018 May ; 65(5): 1095–1106. doi:10.1109/TBME.2017.2741107.

Stimulation Efficiency with Decaying Exponential Waveforms in a Wirelessly-Powered Switched-Capacitor Discharge Stimulation System

Hyung-Min Lee [Member, IEEE],
School of Electrical and Computer Engineering, Georgia Institute of Technology, Atlanta, GA, USA. Now, he is with the School of Electrical Engineering, Korea University, Seoul, South Korea

Bryan Howell [Member, IEEE],
Dept. of Biomedical Engineering, Duke University, Durham, NC. Now, he is with the Department of Biomedical Engineering, Case Western Reserve University, Cleveland, OH, USA

Warren M. Grill, and
Department of Biomedical Engineering, Duke University, Durham, NC, USA

Maysam Ghovanloo [Senior Member, IEEE]
School of Electrical and Computer Engineering, Georgia Institute of Technology, Atlanta, GA, USA

Abstract

The purpose of this study was to test the feasibility of using a switched-capacitor discharge stimulation (SCDS) system for electrical stimulation and subsequently determine the overall energy saved compared to a conventional stimulator. We have constructed a computational model by pairing an image-based volume conductor model of the cat head with cable models of corticospinal tract (CST) axons and quantified the theoretical stimulation efficiency of rectangular and decaying exponential waveforms, produced by conventional and SCDS systems, respectively. Subsequently, the model predictions were tested *in vivo* by activating axons in the posterior internal capsule (IC) and recording evoked electromyography (EMG) in the contralateral upper arm muscles. Compared to rectangular waveforms, decaying exponential waveforms with time constants > 500 μs were predicted to require 2% – 4% less stimulus energy to activate directly models of CST axons and 0.4% – 2% less stimulus energy to evoke EMG activity *in vivo*. Using the calculated wireless input energy of the stimulation system and the measured stimulus energies required to evoke EMG activity, we predict that an SCDS implantable pulse generator (IPG) will require 40% less input energy than a conventional IPG to activate target neural elements. A wireless SCDS IPG that is more energy efficient than a conventional IPG will reduce the size of an implant, require that less wireless energy be transmitted through the skin, and extend the lifetime of the battery in the external power transmitter.

Correspondence to: Hyung-Min Lee; Maysam Ghovanloo.

H.-M. Lee and B. Howell contributed equally to this work.

Index Terms

Implantable pulse generator; stimulation efficiency; switched-capacitor discharging stimulation; wireless power transmission

I. Introduction

Neuromodulation with electrical stimulation is a treatment option for certain neurological diseases and disorders, such as chronic pain, and is used to restore sensory function lost from injury or disease [1]–[3]. One notable example is deep brain stimulation (DBS), which is effective in treating symptoms of movement disorders, such as Parkinson's disease, essential tremor, and dystonia [4]–[6]. The implantable pulse generators (IPGs) used to deliver stimulation are becoming more complex with increasing numbers of channels and functions, including neural recording and closed-loop control [7], [8], which require more energy [9]. This demand for more energy is at odds with making devices smaller and increasing device lifetimes.

Conventional IPGs that use primary cell batteries are limited by large volumes, heavy weights, and limited lifetimes. Because of their size and weight, IPGs used for DBS are implanted in the chest, as opposed to being placed in the skull [10]. This can be problematic as subcutaneous interconnects from the IPG to the electrodes fail due to head motion [11], increasing the number of adverse events. In addition, because the primary cell has a lifetime of approximately 2 – 5 years [12], recipients must incur repeatedly the risks and cost of IPG replacement surgeries [13]. Rechargeable batteries offer an alternative to primary cells. Medtronic's IPGs, the Activa RC neurostimulator for example, has a rechargeable battery that lasts for up to 9 years of operation and has recharge intervals of 2.6 – 42.7 days, depending on stimulation settings [14]. However, rechargeable IPGs are still implanted in the chest due to the battery size, and frequent recharging is burdensome to some patients [14]–[17].

Wireless powering via an inductive transcutaneous link has the potential to enable smaller and longer-lived IPGs. A wirelessly-powered IPG implanted in the temporal bone, similar to a cochlear implant [18], could circumvent the size and longevity constraints of the conventional battery-powered IPG for DBS. However, the power transferred through an inductive link is typically limited due to the small size of the implantable secondary receiver coil [19], and very efficient power management techniques are required to provide sufficient power to the IPG, while reducing the risk of tissue damage from heating [20]. It should be noted that a far-field power transfer, such as electromagnetic radiative transmission as opposed to the near-fiend inductive link, can be optimized in the GHz range considering a small receiving antenna, while prohibited due to large power absorption by body tissues [9].

A wireless switched-capacitor discharge stimulation (SCDS) system can efficiently generate decaying exponential stimuli by coordinating the discharge of storage capacitors into the neural tissue [21]. Decaying exponential waveforms, although not optimally energy efficient for activating neural elements such as neurons and axons, are at least as efficient as rectangular waveforms generated by conventional IPGs [22]–[25]. Because the SCDS

system may be more energy efficient than conventional systems at delivering charge to the tissue [26], and because the use of decaying exponential waveforms does not increase energy requirements compared to rectangular waveforms, we predicted that the overall energy required to stimulate neural elements with an SCDS IPG would be less than required with a conventional IPG.

The goal of this work was to test the feasibility of using an SCDS system for electrical stimulation. The SCDS system architecture used in this work was detailed in [26], in which we presented preliminary computational analyses in a simplified computational model and the results of a pilot *in vivo* experiment. The present work builds upon the previous study by incorporating a significantly more detailed and anatomically accurate model of electrical stimulation, testing the theoretical predictions in a series of *in vivo* experiments, and then using these measurements to compare the performance of the SCDS system to a conventional stimulator. The results indicate that the manner in which the SCDS system delivers charge does not increase the energy requirements for neural activation compared to a conventional system, thus the improvements in energy efficiency for the SCDS system are preserved, resulting in a more energy-efficient system for neuromodulation.

II. Method

A. Switched-Capacitor Discharge Stimulation Mechanism

Conventional stimulation systems require a rectifier and voltage regulator to convert wireless power to a supply voltage and use voltage-controlled stimulation (VCS) to generate rectangular waveforms (Fig. 1a). In contrast, the SCDS system uses a bank of negative (C_N) and positive (C_P) capacitors, first, to store the energy being delivered via induction across the skin from the external battery, and, second, to transfer only the amount of charge required for activation of neural elements (Fig. 1b). The charge stored in the capacitors ($Q = C \times V$) is delivered to the load through low-resistance switches that minimize power loss. Thus, the output from the SCDS system is a decaying exponential voltage/current stimulus (V_{STIM} and I_{STIM}). Table I summarizes the specifications of the wireless SCDS system [26].

B. Model of Electrical Conduction in the Cat Head

1) Image processing—A bioelectric field model was constructed from a 3 Tesla, T1-weighted (T1w) magnetic resonance (MR) image of the cat head [27] and solved using the finite element method (FEM). We used the image-processing software Seg3D [28] to segment the T1w MR image into three regions representing the brain, the portion of the skull surrounding the brain, and a lumped soft-tissue region (Fig. 2). We began by creating a binary mask of the whole head. The raw image was processed with a median filter (radius = 3), and a mask was created by thresholding the filtered image between intensities of 30 and 765. The holes at the nasal cavity, esophagus, and trachea were filled using the flood-fill algorithm in Seg3D. Next, we segmented the brain region using Ostu's method to divide the raw image into two regions and the background [29]. Because the mask that contained the brain also contained portions of the skull and other tissue regions, we first used a rectangular prism that circumscribed the brain to exclude coarsely non-brain regions, and the surface of the brain was determined iteratively. (1) The intended brain mask was dilated and eroded by

a factor of 1 and 2k, where k is the repeat number (see below); (2) the mask from step 1 was dilated by a factor of 4; and (3) the flood-fill algorithm was used to fill any holes in the mask from step 2. Steps 1–3 were repeated five times. The mask of the skull was constructed by dilating the brain mask by a factor of 3, and the mask of the lumped soft-tissue region was constructed by subtracting the masks of the brain and skull from the mask of the whole head.

2) Bioelectric field model—The three binary masks were used to construct a volume-conductor model of the cat head. First, tessellated triangular meshes that bounded the binary masks were constructed in Seg3D and processed in MeshLab (meshlab.sourceforge.net). We applied a sequence of filters to the surface meshes: (i) Quadratic Edge Collapse Decimation was used to reduce the number of faces by 50%; (ii) Laplacian smoothing with surface preservation was used to smooth the decimated mesh; (iii) steps i and ii were repeated until the mesh consisted of 800–1000 faces; and, (iv) 4–8 Subdivision was used to convert the triangular mesh into a quadrilateral mesh.

Second, we used the quadrilateral surface meshes to construct volumes of the corresponding head regions. The non-uniform rational basis spline (NURB) toolbox in MATLAB (v2014b, MathWorks, Natick, MA) was used to convert the quadrilateral meshes to NURBs, and the NURBs, in turn, were used to define closed volumes in COMSOL Multiphysics v5.1 (COMSOL Inc., Burlington, MA).

Third, we constructed a model of an electrode array with a single cylindrical contact (Fig. 3a). The model electrode had a radius of 0.635 mm and a height of 1.5 mm. The shaft had a radius of 0.635 mm and was oriented so that its trajectory fell within the range of possible trajectories observed from post-mortem coronal tissue slices [30].

Fourth, we defined the electrical properties of the different head regions. All the tissues were purely resistive and had a homogeneous, isotropic conductivity (σ). The scalar σ of the brain and skull were 0.23 S/m [31] and 0.02 S/m [32], respectively; and the conductivity of the lumped region of soft tissues was 0.33 S/m. We chose 0.33 S/m, which is the median conductivity of muscle between 1 kHz and 10 kHz [33], because a majority of the soft-tissue volume is comprised of muscles and tendons. The *in vivo* experiments conducted in this study were acute, and for that reason, we ignored the presence of the encapsulation layer surrounding the electrode.

Fifth, we constructed a tetrahedral volume mesh in the model head and used the FEM to solve Laplace's equation.

$$\nabla \cdot (\sigma(x, y, z) \cdot \nabla \Phi) = 0 \quad (1)$$

The dura and arachnoid maters were modeled using a Robin boundary condition at the boundary between the skull and brain:

$$\hat{n} \cdot \sigma^* \cdot \nabla \Phi = \sigma_b \cdot h^{-1} \cdot (\Phi_1 - \Phi_2) \quad (2)$$

, where h is the thickness of the boundary, and Φ_1 and Φ_2 are the potentials on either side of the boundary. h was 2.3 mm, and σ_b = 0.03 S/m [34].

We approximated the temporal variation in the potentials throughout the tissue by defining an equivalent three-element Randles circuit of our computational model [35], [36], solving for the voltage drop across the tissue load (V_{out}) for a given applied waveform (V_{in}), and multiplying the static solution by V_{out}:

$$\Phi(x, y, z, t) = \Phi(x, y, z, t = 0) \times V_{out}(t) \quad (3)$$

The equivalent Randles circuit consisted of a parallel combination of a double-layer capacitance (C_{dl}) and Faradaic resistance (R_f), which represented the electrode-tissue interface (ETI), in series with an access resistance (R_a) that represented the tissue. The relationship between V_{in} and V_{out} satisfied the following ordinary differential equation:

$$C_{dl}V'_{in} + R_f^{-1}V_{in} = C_{dl}V'_{out} + (R_f^{-1} + R_a^{-1})V_{out} \quad (4)$$

, where C_{dl} was calculated by multiplying a specific double-layer capacitance (c_{dl}) by the area of the electrode, and R_f was calculated by dividing a specific Faradaic resistance (r_f) by the area of the electrode. We chose an r_f of 150 kΩcm^2 and a c_{dl} of 30 μF/cm^2, which were determined by fitting solutions of (4) to measured waveforms from previous *in vivo* experiments [30]. An electrode area of 5.98 mm^2 yielded R_f = 2.5 MΩ and C_{dl} = 1.8 μF.

A fixed potential of 1 V (i.e., a Dirichlet boundary condition) was imposed on the active contact. The counter electrode in the *in vivo* experiments (Section 2.2) was a large-area stainless steel surgical retractor atop the head; therefore, no current was allowed to pass through the outer surface of the model cat head, except at the superior boundary of the head, which had a fixed potential of 0 V. The model was solved using ~570,080 third-order elements (~1.9 million degrees of freedom). Refinement of the mesh changed the interpolated potentials and subsequent stimulation thresholds by < 1% with respect to the same values prior to refinement.

3) Models of corticospinal tract (CST) axons—The NEURON (v7.3) simulation environment [37] was used to implement cable models of myelinated axons in the CST. We started with a validated model of a mammalian motor axon [38] and revised its geometry to reflect better the morphology of axons found in the brain. A summary and justification of the geometry of the axon is found a prior work [36].

The trajectory of the CST in the right hemisphere was defined by locating anatomical structures in the T1w MR image [27] and fitting a smoothing spline to a series of control points in the MR image. The following are the anatomical (*x, y, z*) coordinates that we selected from the MR image. We defined one point in the coronal sulcus of the right primary motor cortex, (4.38, −17.86, 0.00); four points in the right internal capsule, (1.88, −25.46, −5.80), (−1.04, −29.06, −0.80), (0.21, −31.86, −1.20), (−2.29, −32.66, −0.38); and two

points in the right pyramid, (−5.20, −43.86, −18.72), (−6.30, −45.46, −25.38). All units are in mm.

The boundaries of the CST were defined using a series of 20 circles along the smoothing spline. In the cat, the internal capsule spans 2 – 3 mm [39], so all circles had a radius of 3 mm. The circles were oriented so that their corresponding normal vectors were collinear with the tangent vectors at the 20 locations along the smoothing spline. Sets of 100 random points were uniformly distributed in all 20 circles, and the points were connected so that the axons maintained their topographical organization across all circles (Fig. 3c)

C. Computational Analyses

The 300 CST axons were stimulated with rectangular and decaying-exponential waveforms (Fig. 3b). Rectangular waveforms had a short cathodic phase followed by a long anodic phase, similar in design to the waveforms used in implantable stimulators. We used three combinations of pulse widths (PWs): cathodic and anodic phases in these three pulses were 100 μs and 900 μs, 300 μs and 700 μs, or 500 μs and 500 μs, respectively. The PWs of the decaying-exponential waveforms were the same as those of the rectangular waveforms. The time constants (τ) of the decaying-exponential waveform were 100 μs, 500 μs, or 1000 μs. These values encompassed the range of τ produced by the SCDS system with a storage capacitance of either 2 μF or 10 μF, a double layer capacitance (C_{dl}) between 0.4 μF and 2.4 μF, a Faradaic resistance (R_f) between 21 kΩ and 8.2 MΩ, and an access resistance (R_a) between 400 Ω and 2 kΩ (Fig. 1b) [30]. With these values, τ was between 134 μs and 3860 μs, while τ larger than 1000 μs led to negligible changes in decaying exponential waveforms considering the relatively short PWs (< 500 μs). Detailed equations can be found in the Appendix.

The interpolated potentials were used to stimulate model CST axons with a train of 30 pulses at 244 Hz. Because (1) is linear, the solution at any given amplitude was calculated by multiplying the solution at 1 V by a scalar, and a bisection algorithm (relative error tolerance < 1%) was used to quantify the stimulation threshold energies of three independently sampled populations of 100 CST axons. An axon was defined as active when at least one action potential reached both of its ends. The injected charge and peak amplitude were also quantified.

D. In Vivo Experiments

Acute experiments were conducted in four anesthetized adult male cats using a protocol approved by the Institutional Animal Care and Use Committee at Duke University. Anesthesia was induced with ketamine HCL (Ketaset 35 mg/kg IM, supplemented as required at 15 mg/kg during surgical preparation). During brain surgery, 1% isoflurane was administered using a vaporizer; and after the surgery, anesthesia was maintained with alpha-chloralose (65 mg/kg IV, supplemented at 15 mg/kg). A 1 cm craniotomy was made, and the dura was reflected, exposing the cortex. We implanted an electrode array in the right hemisphere with stereotactic neurosurgical technique and used a single electrode to deliver rectangular and decaying-exponential stimuli from the conventional and SCDS systems, respectively.

The electrode array was built by wrapping a planar polyimide substrate around a 1.28 mm steel shaft. Electrodes were formed by sputter depositing a chrome adhesion layer followed by a gold metal layer onto the polyimide substrate. The electrode used in this study had a height of 1.5 mm, but a 0.1 mm arc on the substrate was left bare for binding the substrate. Therefore, the active electrode had a surface area of 1.5 mm × 1.27 mm, which was equal to the area of the active electrode in the model. For further details, see “the standard electrode” used in [30].

The VCS system was a hardwired analog isolated stimulator (ASI Model 2220, A-M Systems, Carlsborg, WA). Rectangular waveforms were asymmetric biphasic pulses with a 272 μs cathodic phase followed by a 728 μs anodic phase, and a total of 30 pulses were delivered at 244 Hz. The stimulus pulses were controlled with a high-speed digital-to-analog converter using the DAQ toolbox in MATLAB.

The SCDS system received wireless power and data through an inductive link. Stimulation trains from the SCDS system consisted of 30 asymmetric biphasic pulses with a 272 μs decaying exponential cathodic phase followed by a 900 μs anodic phase. The second phase with the SCDS system was 172 μs longer than that of the VCS system because the former used a stimulus current limiter to regulate the peak amplitude of anodic phase stimulus while ensuring charge-balanced stimulation. Storage capacitor banks, which had combined capacitance of 2 μF or 10 μF, were charged to ±1 V; and pulse trains were delivered at 244 Hz. Charged to the same voltage level, both capacitances resulted in peak stimulation voltage of −1 V. The smaller 2 μF capacitance had a smaller decaying time constant (τ = 504 μs) than the larger 10 μF capacitance (τ = 945 μs). While the SCDS system generates decaying exponential voltage and current waveforms, the impedance range of the ETI is required to estimate the shape of the stimulus, including the peak current amplitude and the time constant [26].

Stimuli were delivered to the posterior limb of the internal capsule (IC; 7 mm anterior, 10.5 mm lateral, and 10 mm above the interaural line [40], [41]), which contains corticospinal and corticobulbar axons projecting from the motor cortex to the spinal cord [42]. Charge passed through the stimulation electrode (Fig. 4) and to a stainless-steel retractor with one end placed below the dura mater and adjacent to the surface of the left cortex. Stimulus currents were measured from voltage drops across a 25 Ω resistor in series with the active electrode, which was low-pass filtered with a cutoff at 100 kHz. Activation of axons in the posterior IC was assessed by recording electromyographic (EMG) activity evoked in the contralateral extensor digitorum (communis and lateral) muscles. The EMG was the differential voltage measured between two 29-gauge multi-strand stainless steel wires (Cooner Wire, Chatsworth, CA) implanted in the arm muscles. The EMG was bandpass filtered from 3 Hz to 3 kHz and amplified by between 100 and 500 (SR560, Stanford Research, Sunnyvale, CA). Data were acquired using the MATLAB 2013b Data Acquisition (DAQ) toolbox (MathWorks, Natick, MA).

The SCDS system was limited to peak amplitudes between ± 0.4 V and ± 1.5 V, inclusive, with a resolution of 0.1 V. Therefore, we tested twelve unique amplitudes, each of which was repeated five times, for a total of 60 pulse trains. The order of the pulse trains was

randomized for each trial. At each stimulus amplitude, we calculated the integral of the rectified EMG (*IRE*), and the stimulus energy and injected charge were calculated from the measured transient stimulus voltage and current over time.

A smoothing spline fit to the experimental data was used to interpolate the peak voltage amplitude, stimulus energy, and injected charge required to produce a half maximal *IRE*. The stimulus energies required to evoke a half maximal *IRE* ($E_{IRE,50}$) in response to SCDS and VCS were analyzed with a repeated measures analysis of variance (ANOVA), which tested the null hypothesis that the mean $E_{IRE,50}$ for both cases were the same. All statistical tests were performed at $\alpha < 0.05$. The stimulation threshold energies, E_{STIM}, of the SCDS (i.e., $E_{IRE,50}$) were normalized by dividing with those from the VCS experiments, log transformed to give equal weight to values above and below 1, and averaged ($n = 4$) to calculate the relative stimulation energy ratio of SCDS, f_{STIM}, compared to VCS:

$$f_{STIM} = exp\left(\frac{log\left(\frac{E_{STIM,SCDS,1}}{E_{STIM,VCS,1}}\right) + \ldots + log\left(\frac{E_{STIM,SCDS,n}}{E_{STIM,VCS,n}}\right)}{n}\right) \quad (5)$$

E. Estimation of Overall Energy

We used measurements of system efficiencies from previous work [26], [43]–[46] and the stimulus energies measured from the *in vivo* experiments to estimate the overall energy required with the wireless SCDS system (Fig. 1b) compared to a wireless VCS system (Fig. 1a). The overall relative energy savings of the SCDS system relative to the VCS system was quantified using the ratio:

$$ESR_{SCDS} = 1 - \frac{E_{IN,SCDS}}{E_{IN,VCS}} \quad (6)$$

where $E_{IN,SCDS}$ and $E_{IN,VCS}$ are the input energies of the SCDS and VCS systems, respectively. The efficiency of a system (η) is typically expressed as the ratio of the output to the input energy. Therefore, (6) can be rewritten as

$$ESR_{SCDS} = 1 - \frac{\frac{E_{STIM,SCDS}}{\eta_{SYS,SCDS}}}{\frac{E_{STIM,VCS}}{\eta_{SYS,VCS}}} \quad (7)$$

where $E_{STIM,SCDS}$ and $E_{STIM,VCS}$ are the output energies of the SCDS and VCS systems, respectively, and are the corresponding $E_{IRE,50}$ from the *in vivo* experiments; and $\eta_{SYS,SCDS}$ and $\eta_{SYS,VCS}$ are the corresponding system efficiencies. Finally, substitution of (5) into (7) yields,

$$ESR_{SCDS} = 1 - \frac{\eta_{SYS,VCS}}{\eta_{SYS,SCDS}} f_{STIM} \quad (8)$$

For a fair comparison of system efficiencies, we assumed that both the SCDS and VCS systems operated at the same supply voltage of ±2.1 V. In the VCS system, the system efficiency was a product of energy efficiencies of a rectifier [43], a regulator, and a voltage stimulator (Fig. 1a). Regulator input and output voltages were ±2.3 V and ±2.1 V, respectively; and ignoring internal power consumption, a low-dropout (LDO) regulator efficiency was derived by dividing the regulator output voltage by the input voltage. Assuming that the voltage stimulator used a buffer amplifier [44], [45] the stimulator efficiency was estimated as the output power over the input power of the stimulator, which is equivalent to the stimulus amplitude over the supply voltage during the stimulation phase. Internal power consumption of the stimulator was ignored in the calculation. In the SCDS system, the system efficiency was a product of charging efficiency of storage capacitors [46] and discharge efficiency into the neural tissue [26] (Fig. 1b).

III. Results

We used an image-based computational model of electrical stimulation in the cat brain to quantify the stimulation efficiency of rectangular and decaying exponential waveforms. The predictions of the model were tested *in vivo*, and we used the results from the *in vivo* experiments and prior studies to estimate the overall energy required with the wireless SCDS system compared to a conventional VCS system.

A. Computational Simulation of Stimulation Waveform Effects

For all PWs tested, the energy required to activate 50% of model CST axons differed by < 7% between the rectangular and decaying exponential pulses (Fig. 5a). As the PW increased, decaying exponential waveforms with τ of 500 μs and 1000 μs were more efficient than rectangular waveforms, but energy savings were relatively small (< 4%). Only the decaying exponential waveform with a τ of 100 μs was less efficient for all PWs except 500 μs.

The decaying exponential waveforms with the shortest τ required less injected charge than rectangular pulses and decaying exponentials with longer τs (Fig. 5b). As PW increased, decaying exponential waveforms with shorter τs required higher peak stimulus voltage (Fig. 5c) than rectangular pulses. The relative efficiencies were not sensitive to the choice of the proportion of the population of models axons that was activated. For example, the normalized stimulus energies for activation of 25%, 50%, 75%, and 100% of the CST axons had a standard deviation of < 0.7% across all cases tested (Fig. 5d).

B. Stimulation Efficiencies of SCDS and VCS Systems In Vivo

Evoking a half maximal *IRE* with the SCDS system required 10% larger voltage amplitudes than the VCS system (Fig. 6a and 7), consistent with model predictions (Fig. 5c). The $E_{IRE,50}$ of the SCDS system with storage capacitances of 2 μF (τ = 504 μs) and 10 μF (τ = 945 μs) was less than that of the VCS system by 2% and 0.4%, respectively (Fig. 6b and 7),

based on (5), and these efficiencies were similar to model predictions (Fig. 5a). The statistical comparison between the SCDS and VCS systems verified that stimulation threshold energies and charges were not significantly different across the three stimulus waveforms.

C. Calculation of Overall Energy

The voltage applied to a VCS system has three stages where losses occur: the rectifier, the regulator, and the voltage stimulator (Fig. 1a). A properly-designed rectifier has an average efficiency of ~80%, considering variations in input voltage amplitude, output load, and carrier frequency [43], and a low-dropout regulator has an average efficiency of 77.8% (= ±2.1 V / ±2.7 V) with the dropout voltage of 0.6 V to accommodate with input voltage and load variations. We estimated that the efficiency of the voltage stimulator using the buffer amplifier would be 43.3% (= −0.91 V / −2.1 V) with an average cathodic stimulation amplitude of −0.91 V from experiments. We also estimated that the system efficiency of the VCS system was 27%. A dynamic supply voltage stimulator in [47] achieved a higher efficiency of 52 – 94% at the expense of coarse stimulation voltage/current controllability. Nonetheless, it still required a rectifier and a regulator to convert wireless ac power to dc input voltage, decreasing the overall system efficiency to 45.4%.

A SCDS system, in contrast, has two stages where losses occur: the charging and discharging of the storage capacitors. The charging process has an efficiency of 62% [46], the discharging process has an efficiency of 95%, most of which is due to losses in the switches [26], for an average cathodic stimulation peak amplitude of −1.07 V from experiments. The product of these two efficiencies gives a system efficiency of 58.9% for the SCDS system.

The relative stimulation energy ratio, f_{STIM}, based on (5) across the four *in vivo* experiments was 0.98. Therefore, the SCDS system required 59.3% of the input energy of the VCS system, from input to output, which corresponds to an energy saving ratio of 40.7%, according to (8). It is also possible that the true f_{STIM} is smaller than what was measured. In the worst case scenario, f_{STIM} would be 1, but the energy saving ratio of the SCDS system is still 39.5%, from the instrumentation alone.

One corollary of the above is that compared to a VCS system, an SCDS system can activate a larger volume of tissue for a given input energy (i.e., before losses). This is because for decaying exponential waveforms with $\tau \geq 500$ μs, the stimulation threshold energy required to stimulate axons with an SCDS system is less than or equal to that of a VCS system, and energy losses in an SCDS system are less than that of a VCS system. For example, when stimulation threshold energy was matched between the SCDS and VCS systems, the model predicted that decaying exponential waveforms with $\tau = 500$ μs activated 64%, 65%, and 67% of the CST axon population with 100 μs, 300 μs, and 500 μs pulses, respectively, leading to a 28 – 34% increase in axon activation over the VCS system (50% axon activation). Similar trends were observed in the experimental data when factoring in energy losses, leading to 60 – 80% higher *IRE* compared to the half maximal *IRE* generated by the VCS system at the same input energy.

IV. Discussion

We combined computational modeling and *in vivo* experiments to compare the stimulation efficiency of an SCDS system to that of a VCS system. The modeling and *in vivo* results suggest that an SCDS system with decaying exponential waveforms can perform on par with a VCS system, with regard to stimulation of neural elements. Because the wireless SCDS system required less input energy than the VCS system to inject the same amount of charge for a given load, the SCDS system reduced overall energy requirements compared to a conventional VCS system.

A. The Energy Efficiency of Decaying Exponential Waveforms

The efficiency of a decaying exponential waveform compared to a rectangular waveform can be explained by considering the timing and amplitude of the stimulus voltage in relation to the dynamics of the voltage-gated ion channels in the neural membrane [23]. The threshold for evoking an action potential depends primarily on the excitability of the fast sodium channels, whose dynamic conductance in our axon model was proportional to a state inactivation variable, h, and the cube of a state activation variable, m. Depolarization of the membrane activates the m-gate (i.e., m increases) and inactivates the h-gate (i.e., h decreases), but inactivation is an order of magnitude slower than activation. Given the counteracting forces of theses gates and their different time courses, one can envision a time window when the membrane is the most excitable, thereby waveforms whose amplitudes are maximal earlier and progressively decrease as h inactivates are expected to be more energy-efficient than waveforms with constant amplitudes.

The dynamics described above depended on the duration of the waveform. For PWs ≤ 300 μs, the process of activation (i.e., m increasing) dominated because there was little time for inactivation to occur. The decaying exponential waveform with $\tau = 100$ μs decayed too rapidly and did not depolarize the membrane as efficiently as the near constant decaying exponential waveforms or constant rectangular waveforms. However, as PW increased above 300 μs, the amount of inactivation was no longer negligible, and it became advantageous to decrease progressively the amplitude of the applied waveform over time. This explains why decaying exponential waveforms became more efficient as PW increased and why the decaying exponential with the smallest time constant was less efficient at shorter PWs.

B. Energy-Efficient Wireless Systems with SCDS

Efficient wireless stimulation requires not only a system that uses less energy to deliver charge to the neural tissue but also stimulus waveforms that can activate target neural elements using less energy. The wireless SCDS system-on-a-chip offers high efficiency and has the potential to reduce the size of the IPG by using banks of small surface-mount (SMD) storage capacitors to store and deliver charge. Furthermore, if implemented in a high voltage CMOS process for stimulation applications that need higher energy or peak amplitude in stimulus waveforms, the efficiency of the SCDS system can be further increased when capacitors are charged to higher voltages, as a result of higher capacitor charging efficiency [46]. This is primarily because the losses and dropout voltages become a smaller percentage

of the overall operating voltage or stimulus amplitude. This will result in more power delivered to the tissue (a desired outcome) and thus higher efficiency of the SCDS system.

In addition, assuming that the practical range of the time constants for decaying exponential stimuli are between 500 μs and 1000 μs, the SCDS system requires only 10 – 20% higher peak voltages than rectangular stimuli of equal duration (Fig. 5 and Fig. 7), which results in tolerable changes in the wireless power link. The current SCDS prototype uses the unlicensed 2 MHz band to achieve high efficiency in a large feature-sized standard CMOS process (0.35-μm). The wireless IPG that uses this SCDS prototype can be powered from a behind-the-ear transmitter, similar to cochlear implants, through a closely-coupled transcutaneous wireless link [2]. In the case of incorporating a rechargeable battery to maintain system powering during occasional loss of wireless power, a battery charging circuit can be added to the existing rectifier and regulator of the SCDS system (the power control block in Fig. 1) similar to conventional stimulation systems. The effect of a small battery charging current on the overall stimulation efficiency would be negligible.

The SCDS system currently generates decaying exponential stimuli, but other more energy-efficient stimulus waveforms, similar to truncated sinusoids or Gaussian waveforms [48], are possible using several pairs of storage capacitors. For more flexible stimulus waveforms, the charge storage capacitors of the SCDS system can be programmed to various voltages and sequentially connected to the output, generating, for example, a pseudo-rectangular or ramp stimulus [49]. However, the number of off-chip storage capacitors may limit the waveform resolution and affect the implant size. Considering the size of the smallest commercial 1 – 4.7 μF SMD capacitor ($1 \times 0.5 \times 0.3$ mm^3) [50] in comparison to the size of the current prototype SCDS chip ($5 \times 2.4 \times 0.3$ mm^3), it is feasible to use 4 – 8 pairs of capacitors located on the opposite side of the PCB, against the SCDS chip, thereby minimizing the increase in footprint due to off-chip capacitor banks. In this SCDS prototype, storage capacitors of 1 μF, 1 μF, 3.3 μF, and 4.7 μF were chosen so that 4 pairs of capacitors (with a total capacitance of 10 μF) could be fully charged to ±1.5 V within 2.5 ms to operate at a stimulation rate of at 244 Hz and transfer charge up to 3.7 μC to the load (i.e., tissue) during the 272 μs cathodic phase [51]. The storage capacitors in the SCDS system did not require values above a few μF since each capacitor stored only the amount of charge needed for a single stimulus (e.g. < a few μC). The current SCDS prototype can be shrunk further by removing test components on the PCB and integrating the receiver coil, L_2, into the PCB [52].

We used ceramic capacitors in the proof-of-concept prototype for acute *in vivo* testing and characterization. However, the capacitance of ceramic capacitors may change (up to 20%) depending on the applied DC voltages. Therefore, tantalum capacitors [53], which are much more stable over the DC voltages and resistant to aging may be a more appropriate choice for a medical grade SCDS. Tantalum is also more stable against temperature variations than ceramic capacitors, even though the IPG temperature changes are expected to be small, particularly after implantation.

C. Advantages of an SCDS system

The IPG with the SCDS system aims for two primary goals:

1. Size reduction: Wireless powering enables smaller IPGs by removing implanted batteries. Although the SCDS system used off-chip capacitor banks, they are smaller (< mm^3/each) than primary or rechargeable batteries (> several cm^3) and can be located on the opposite side of the SCDS chip, minimizing the increase in footprint.

2. Power efficiency: The amount of power consumed in the IPG is typically limited due to the risk of tissue damage from temperature rise. For example, the power density of the chip needs to be well below 800 μW/mm^2 (i.e., 9.6 mW in our 5 × 2.4 mm^2 SCDS chip) to prevent tissue damage [54], [55]. However, IPGs, such as Medtronic's neurostimulators in [14], provide maximum instantaneous and average power of up to 8 mW and 1.8 mW per channel, respectively, when injecting 2 V biphasic stimuli to 500 n electrodes for 450 μs at 250 Hz. The limited input power should be efficiently transferred to electrodes by dissipating minimum power in the IPG. The SCDS system can generate sufficient stimuli by receiving less wireless power. It also increases the lifetime of the battery in the external power transmitter.

Standard wireless stimulation systems are often designed based on either VCS or current-controlled stimulation (CCS). A shortcoming of VCS is its inability to control the injected charge, which poses an issue because the load in electrical stimulation therapies has a broad range and may vary over time [45], [56]. CCS, on the other hand, offers precise charge control regardless of the load, but at the expense of inherent inefficiency. In CCS, additional power losses occur across the current source/sink transistors in stimulators, particularly when the stimulation voltage level or electrical load is low [47], [57]. A wireless CCS system also requires a rectifier and regulator in the power management block to generate a system supply voltage that should remain stable, despite coupling variations (Fig. 1a). Moreover, CCS typically requires a higher supply voltage to accommodate the wide range of stimulation voltages (i.e., 1 – 10 V) that are used in clinical stimulators. At higher stimulation compliance voltages, a charge-pump regulator or boost DC-DC converter can be used to generate higher supply voltages, at the cost of additional power losses and space requirement of on-chip real estate, increasing the fabrication cost. Therefore, although CCS addresses the aforementioned limitation of VCS, this comes at the expense of a substantial reduction in power efficiency compared to a VCS system [18].

The SCDS system controls the amount of charge injected into the tissue instead of controlling the amount of current. The SCDS system first stores the energy that is wirelessly delivered across the skin from the external battery to a capacitor bank, and second, it transfers the stored charge to the neural tissue. As the storage capacitors discharge, the voltage decays over time, so the injected charge is simply the product of the storage capacitance and the difference in voltage before and after stimulation. Direct control of the charged and discharged voltage levels not only improves power efficiency, by creating a buffer between the inductive link and the highly variable load without using any rectifiers or regulators [46], but also ensures highly efficient and charge-balanced stimulation, regardless of the load variations. Therefore, the SCDS system has benefits of both VCS and CCS

systems. Table II benchmarks the wireless SCDS system against conventional and state-of-the-art VCS/CCS systems in the literature.

D. Study Limitations

The computational model constructed in this study used a high-resolution T1 MR image of the cat head to model, as closely as possible, the *in vivo* experiments. The image-based model accurately represented the dimensions of the head and brain and accounted for changes in electrical conductivity between these three regions. However, additional electrical complexities that were not modeled could affect the model predictions. For example, we ignored heterogeneity and anisotropy present within the brain tissue, which has a marked effect on predictions of stimulation thresholds [36]. Although the piecewise homogeneous model may misestimate the stimulation thresholds compared to a model that incorporates anisotropy and heterogeneity, we predict that the relative trends we observed will be similar in a more complex model. That is, the errors in absolute threshold are expected to be approximately the same for both rectangular and decaying exponential waveforms.

Further, we used anatomical information from the MR image to estimate the trajectory of descending corticospinal and corticobulbar axons, which were the target neural elements during the *in vivo* experiments. A more accurate estimate of the trajectories of the modeled axons could be obtained by conducting deterministic or probabilistic tractography, but given the lack of availability of diffusion MR images of the cat brain, as well as the toolboxes for processing these types of images, tractography was not conducted in this study.

Finally, the study included a limited number of experiments. The model predicted that an SCDS system (decaying rectangular waveforms with $\tau \geq 500$ μs) would require as much as 4% less energy than a VCS system (rectangular waveforms) to stimulate passing axons. Four *in vivo* experiments were enough to confirm that the average stimulation threshold energy difference between the SCDS and VCS systems was small (< 2%). However, using the standard deviation of the difference in $E_{IRE,50}$ across the four experiments, we estimated that 200 experiments would be required to show that this effect was statistically significant (α = 0.05). Rather than committing a large amount of resources to discern such a small effect in an acute setting, we recommend that the SCDS system be tested in chronic experiments, thereby giving a more direct indication of its prospective performance as a chronic stimulator.

V. Conclusion

Efficient wirelessly-powered stimulation requires not only a system that uses less input energy to transfer energy across the skin and deliver charge to the neural tissue but also stimulus waveforms that are equally or more energy efficient at stimulating neural elements than conventional rectangular waveforms. The wireless SCDS system is capable of both transferring energy to charge an array of small SMD capacitors efficiently and delivering charge stored in those capacitors to the neural tissue in a manner that consumes less power than a conventional VCS system. We successfully tested the feasibility of using an SCDS system to activate neural elements in the brain using less energy than a conventional stimulator. An IPG with the efficient wireless SCDS system will enable size reduction of an

implant, less wireless energy transmission through the skin (and thereby less heat dissipation), and longer battery life of the external power transmitter, such as behind-the-ear devices.

Acknowledgments

The authors thank Case Western Reserve University for use of the High Performance Computing Resource.

This work was supported by F32 NS096839, R01 MH102238, R21 EB018561, and R37 NS040894 from the National Institutes of Health as well as ECCS-0824199 from the National Science Foundation.

Appendix

The time constants for the waveform generated by the SCDS system (shown in Fig. 1b) were approximated using a four-element circuit, where C_S is the storage capacitance, C_{dl} is the double-layer capacitance, R_f is Faradaic resistance, and R_a is the access/tissue resistance. The second-order ordinary differential equation (ODE) that describes the temporal dynamics of voltage drop (V_S) across the load is given by the following equation:

$$aV_{S,t'} + bV_{S,t} + cV = 0 \quad \text{(A.1)}$$

$$a = C_S C_{dl} R_a \quad \text{(A.2)}$$

$$b = C_S + C_{dl} + C_S R_a / R_f \quad \text{(A.3)}$$

$$c = 1/R_f \quad \text{(A.4)}$$

, where the subscripts t and t' denote the first and second time derivatives of V_S, respectively. The roots of the characteristic polynomial associated with (A.1) were calculated by solving the quadratic equation, and the time constants, τ_1 and τ_2, are the negative reciprocal of the roots:

$$\tau_{1,2} = -2a/(-b \pm \sqrt{(b^2 - 4ac)}) \quad \text{(A.5)}$$

We defined the effective rate of decay as the minimum of τ_1 and τ_2. Storage capacitances of 2 μF and 10 μF were considered in this work, and ranges for the other circuit elements are 0.4 μF ≤ C_{dl} ≤ 2.4 μF, 21 kΩ ≤ R_f ≤ 8.2 MΩ, 0.4 kΩ ≤ R_a ≤ 2 kΩ [30]. Given these ranges, the rate of decay can be as small as 134 μs and as large as 3.86 ms. However, with the SCDS

system, we only observed rates of decay of between 400 μs and 1000 μs in the *in vivo* experiments, so we considered a smaller range of values in our modeling analysis.

References

1. Johnson M, Martinson M. Efficacy of electrical nerve stimulation for chronic musculoskeletal pain: A meta-analysis of randomized controlled trials. PAIN. Jul.2007 130(1–2):157–165. [PubMed: 17383095]
2. Wilson BS, Dorman MF. Cochlear implants: A remarkable past and a brilliant future. Hearing Res. Aug.2008 242(1–2):3–21.
3. Cruz LD, Coley BF, Dorn J, Merlini F, Filley E, Christopher P, Chen FK, Wuyyuru V, Sahel J, Stanga P, Humayun M, Greenburg RJ, Dngnelie G. The Argus II epiretinal prosthesis system allows letter and word reading and long-term function in patients with profound vision loss. Br. J. Ophthalmol. May; 2013 97(5):632–636. [PubMed: 23426738]
4. Fasano A, Daniele A, Albanese A. Treatment of motor and non-motor features of Parkinson's disease with deep brain stimulation. Lancet Neurol. May.2012 11:429–442. [PubMed: 22516078]
5. Lyons KE, Pahwa R. Deep brain stimulation and tremor. Neurotherapeutics. Apr.2008 5(2):331–338. [PubMed: 18394574]
6. Vercueil L, Pollak P, Fraix V, Caputo E, Moro E, Benazzouz A, Xie J, Koudsie A, Benabid A-L. Deep brain stimulation in the treatment of severe dystonia. J. Neurology. Aug.2001 248(8):695–700.
7. Ghovanloo, M. Integrated circuits for neural interfacing: Neural stimulation. In: Iniewski, K., editor. VLSI Circuits for Biomedical Applications. Norwood, MA: Artech House; 2008.
8. Afshar P, Khambhati A, Stanslaski S, Carlson D, Jensen R, Linde D, Dani S, Lazarewicz M, Cong P, Giftakis J, Stypulkowski P, Denison T. A translational platform for prototyping closed-loop neuromodulation systems. Frontiers in Neural Circuits. Jan.2013 6:1–15. article 117.
9. Rasouli M, Phee LS. Energy sources and their development for application in medical devices. Expert review of Medical Devices. Sep.2010 7(5):693–709. [PubMed: 20822391]
10. Moore SK. Psychiatry's shocking new tools. IEEE Spectrum. Mar.2006 43(3):24–31.
11. Farris S, Giroux M. Deep brain stimulation: A review of the procedure and the complications. J. Am. Acad. Physician Assist. Feb.2011 24(2):39–45.
12. Dorval AD, Kuncel AM, Birdno MJ, Turner DA, Grill WM. Deep brain stimulation alleviates parkinsonian bradykinesia by regularizing pallidal activity. J. Neurophysiol. Aug.2010 104(2): 911–921. [PubMed: 20505125]
13. Voges J, Waerzeggers Y, Maarouf M, Lehrke R, Koulousakis A, Lenartz D, Sturm V. Deep-brain stimulation: long-term analysis of complications caused by hardware and surgery - experiences from a single centre. J. Neurol. Neurosurg. Psychiatry. Jul.2006 77(7):868–872. [PubMed: 16574733]
14. System eligibility, battery longevity - Neurostimulation systems for deep brain stimulation. Medtronic; Minneapolis, MN, USA: 2014.
15. Harries AM, Major S, Sandhu M, Honey CR. Rechargeable internal neural stimulators—Is there a problem with efficacy? Neuromodulation: Technology at the Neural Interface. 2012; 15:214–218.
16. Timmermann L, Schüpbach M, Hertel F, Wolf E, Eleopra R, Franzini A, et al. A new rechargeable device for deep brain stimulation: A prospective patient satisfaction survey. European Neurology. 2013; 69:193–199. [PubMed: 23328107]
17. Waln O, Jimenez-Shahed J. Rechargeable deep brain stimulation implantable pulse generators in movement disorders: Patient satisfaction and conversion parameters. Neuromodulation: Technology at the Neural Interface. 2014; 17:425–430.
18. Lee H-M, Park H, Ghovanloo M. A power-efficient wireless system with adaptive supply control for deep brain stimulation. IEEE J. Solid-State Circuits. Sep.2013 48(9):2203–2216. [PubMed: 24678126]
19. Jow U, Ghovanloo M. Design and optimization of printed spiral coils for efficient transcutaneous inductive power transmission. IEEE Trans. Biomed. Circuits Syst. Sept.2007 1(3):193–202. [PubMed: 23852413]

20. Fujii T, Ibata Y. Effects of heating on electrical activities of guinea pig olfactory cortical slices. Eur. J. Physiol. 1982; 392:257–260.
21. Ghovanloo M. Switched-capacitor based implantable low-power wireless microstimulating systems. IEEE Intl. Symp. on Circuits and Systems. May.2006 :2197–2200.
22. Sahin M, Tie Y. Non-rectangular waveforms for neural stimulation with practical electrodes. J. Neural Eng. Sep.2007 4(3):227–233. [PubMed: 17873425]
23. Wongsarnpigoon A, Woock JP, Grill WM. Efficiency analysis of waveform shape for electrical excitation of nerve fibers. IEEE Trans. Neural Syst. Rehab. Eng. Jun.2010 18(3):319–328.
24. Hofmann L, Ebert M, Tass PA, Hauptmann C. Modified pulse shapes for effective neural stimulation. Front. Neuroeng. Sep.2011 4(9):1–10. [PubMed: 21270946]
25. Foutz TJ, Ackermann DM Jr, Kilgore KL, McIntyre CC. Energy efficient neural stimulation: Coupling circuit design and membrane biophysics. PLoS ONE. Dec.2012 7(12)
26. Lee H-M, Kwon K-Y, Li W, Howell B, Grill WM, Ghovanloo M. A power-efficient switched-capacitor stimulating system for electrical/optical deep-brain stimulation. IEEE J. Solid-State Circuits. Jan.2015 50(1):360–374.
27. Gray-Edwards HL, Salibi N, Josephson EM, Hudson JA, Cox NR, Randle AN, McCurdy VJ, Bradbury AM, Wilson DU, Beyers RJ, Denney TS, Martin DR. High resolution MRI anatomy of the cat brain at 3 Tesla. J. Neurosci. Methods. Apr.2014 227:10–17. [PubMed: 24525327]
28. Software [online]. Available: http://www.sci.utah.edu/software/seg3d.html
29. Otsu N. A threshold selection method from gray-level histogram. IEEE Trans. Syst. Man Cybern. Jan.1979 9(1):62–66.
30. Howell B, Huynh B, Grill WM. Design and in vivo evaluation of more efficient and selective deep brain stimulation electrodes. J. Neural Eng. Aug.2015 12(4)
31. Gabriel C, Peyman A, Grant EH. Electrical conductivity of tissue at frequencies below 1 MHz. Phys Med Biol. Aug.2009 54(16):4863–4878. [PubMed: 19636081]
32. Kosterich JD, Foster KR, Pollack SR. Dielectric permittivity and electrical conductivity of fluid saturated bone. IEEE Trans. Biomed. Eng. Feb.1983 30(1):81–86. [PubMed: 6832795]
33. Gabriel S, Lau RW, Gabriel C. The dielectric properties of biological tissues: II. Measurements in the frequency range 10 Hz to 20 GHz. Phys. Med. Biol. Nov.1996 41(11):2251–2269. [PubMed: 8938025]
34. Struijk JJ, Holsheimer J, Barolat G, He J, Boom HBK. Paresthesia thresholds in spinal cord stimulation: A comparison of theoretical results with clinical data. IEEE Trans. Rehab. Eng. Jun. 1993 1(2):101–108.
35. Howell B, Naik S, Grill WM. Influences of interpolation error, electrode geometry, and the electrode-tissue interface on models of electric fields produced by deep brain stimulation. IEEE Trans Biomed Eng. Feb.2014 61(2):297–307. [PubMed: 24448594]
36. Howell B, McIntyre CC. Analyzing the tradeoff between electrical complexity and accuracy in patient-specific computational models of deep brain stimulation. J. Neural Eng. May.2016 13(3)
37. Carnevale, N., Hines, M. NEURON Simulation Environment. In: Jaeger, D., Jung, R., editors. Encyclopedia of computational neuroscience. Springer; Berlin: 2014.
38. McIntyre CC, Richardson AG, Grill WM. Modeling the excitability of mammalian nerve fibers: influence of afterpotentials on the recovery cycle. J. Neurophysiol. Feb.2002 87(2):995–1006. [PubMed: 11826063]
39. Nicholson PW. Specific impedance of cerebral white matter. Exp. Neurol. Dec.1965 13(4):386–401. [PubMed: 5847284]
40. Nicholson PW. Specific impedance of cerebral white matter. Exp. Neurol. Dec.1965 13(4):386–401. [PubMed: 5847284]
41. Snider, RS., Niemer, WT. A stereotaxic atlas of the cat brain. Chicago: University of Chicago Press; 1961.
42. Lemon RN. Descending pathways in motor control. Annu. Rev. Neurosci. Jul.2008 31:195–218. [PubMed: 18558853]

43. Lu Y, Ki W-H. A 13.56 MHz CMOS active rectifier with switched-offset and compensated biasing for biomedical wireless power transfer systems. IEEE Trans. Biomed. Circuits Syst. Jun.2014 8(3): 334–344. [PubMed: 23846494]
44. Shahrokhi F, Abdelhalim K, Serletis D, Carlen PL, Genov R. The 128-channel fully differential digital integrated neural recording and stimulation interface. IEEE Trans. Biomed. Circuits Syst. Jun.2010 4(3):149–161. [PubMed: 23853339]
45. Simpson, J., Ghovanloo, M. An experimental study of voltage, current, and charge controlled stimulation front-end circuitry; Proc. IEEE Intl. Symp. on Cir. and Sys. (ISCAS); May. 2007 p. 325-328.
46. Lee H-M, Ghovanloo M. A power-efficient wireless capacitor charging system through an inductive link. IEEE Trans. on Circuits and Systems-II. Sep.2013 60(10):707–711.
47. Arfin S, Sarpeshkar R. An energy-efficient, adiabatic electrode stimulator with inductive energy recycling and feedback current regulation. IEEE Trans. Biomed. Circuits Syst. Feb.2012 6(1):1–14. [PubMed: 23852740]
48. Wongsarnpigoon A, Grill WM. Energy-efficient waveform shapes for neural stimulation revealed with a genetic algorithm. J. Neural Eng. Jun.2010 7(4)
49. Kelly S, Wyatt J. A power-efficient neural tissue stimulator with energy recovery. IEEE Trans. Biomed. Circuits Syst. Feb.2011 5(1):20–29. [PubMed: 23850975]
50. GRM153R60G475ME15D Datasheet, Murata Electronics North America Inc. [Online]. Available: http://psearch.en.murata.com/capacitor/product/GRM153R60G475ME15%23.pdf
51. Kuncel AM, Grill WM. Selection of stimulus parameters for deep brain stimulation. Clin. Neurophysiol. Nov.2004 115(11):2431–2441. [PubMed: 15465430]
52. Lee, H-M., Kwon, K-Y., Li, W., Ghovanloo, M. A wireless implantable switched-capacitor based optogenetic stimulating system; Proc. IEEE Eng. in Med. and Biol. Conf. (EMBC); Aug.. 2014 p. 878-881.
53. TACK475M003QTA Datasheet, AVX Corporation. [Online]. Available: http://http://datasheets.avx.com/TAC.pdf
54. Karkare V, Gibson S, Markovic D. A 130-μW, 64-channel neural spike-sorting DSP chip. IEEE J. Solid-State Circuits. May; 2011 46(5):1214–1222.
55. Seese TM, Harasaki H, Saidel GM, Davies CR. Characterization of tissue morphology, angiogenesis, and temperature in adaptive response of muscle tissue to chronic heating. Lab. Investigation. 1998; 78(12)
56. Vidal, J., Ghovanloo, M. Toward a switched-capacitor based stimulator for efficient deep-brain stimulation; Proc. IEEE Eng. in Med. and Biol. Conf. (EMBC); Sep.. 2010 p. 2927-2930.
57. Chen K, Yang Z, Hoang L, Weiland J, Humayun M, Liu W. An integrated 256-channel epiretinal prosthesis. IEEE J. Solid-State Circuits. Sep.2010 45(9):1946–1956.
58. Williams I, Constandinou TG. An energy-efficient, dynamic voltage scaling neural stimulator for a proprioceptive prosthesis. IEEE Trans. Biomed. Circuits Syst. Apr.2013 7(2):129–139. [PubMed: 23853295]
59. Kiani M, Ghovanloo M. An RFID-based closed loop wireless power transmission system for biomedical applications. IEEE Trans. Cir. Syst. II. Apr.2010 57(4):260–264.

Biographies

Hyung-Min Lee (M'14) received the B.S. degree in electrical engineering (*summa cum laude*) from Korea University, Seoul, Korea, in 2006, the M.S. degree in electrical engineering from the Korea Advanced Institute of Science and Technology (KAIST), Daejeon, Korea, in 2008, and the Ph.D. degree in electrical and computer engineering from Georgia Institute of Technology, Atlanta, GA, USA, in 2014.

From 2014 to 2015, he was a postdoctoral associate in the Department of Electrical Engineering and Computer Science, Massachusetts Institute of Technology (MIT), Cambridge, MA, USA. From 2015 to 2017, he was with the IBM T. J. Watson Research Center as a Research Staff Member. In 2017, he joined the School of Electrical Engineering, Korea University, Seoul, South Korea, where he is currently an assistant professor. His research interests include analog/mixed-signal/power-management integrated circuit and microsystem design for biomedical, sensor, and IoT applications.

Prof. Lee received Silver Prizes in the 16th and 18th Human-Tech Thesis Prize contest from Samsung Electronics, Korea, in 2010 and 2012, respectively, and the Commendation Award in the 4th Outstanding Student Research Award from TSMC, Taiwan, in 2010.

Bryan Howell received his B.S. degree in biomedical engineering and a Minor in mathematics in 2009 from The University of Michigan in Ann Arbor, and he obtained his Ph.D. in biomedical engineering in 2015 from Duke University in Durham, North Carolina.

He is a Postdoctoral Fellow in the Neuromodulation Center at Case Western Reserve University in Cleveland, OH and currently works alongside a cross-disciplinary team in the Depression Biometrics Lab at Emory University in Atlanta, GA. His research interests are in neural engineering and include neuroimaging, tractography, numerical methods, design and optimization of stimulation techniques for neural prostheses, and applications of computational neuroscience to studying the treatment of movement and psychiatric disorders with deep brain stimulation.

Dr. Howell received the F31 Predoctoral Fellowship from the National Institutes of Health in 2012 and subsequently, the F32 Postdoctoral Fellowship in 2016.

Warren M. Grill is the Edmund T. Pratt, Jr. School Distinguished Professor of Biomedical Engineering at Duke University. He received the B.S. degree in biomedical engineering in 1989 from Boston University and the Ph.D. in biomedical engineering in 1995 from Case Western Reserve University, Cleveland, OH.

He is Co-Founder, Director, and Chief Scientific Officer of NDI Medical, a medical device incubator, Co-Founder, Director, and Chief Scientific Officer of DBI, which is commercializing a novel approach to brain stimulation for neurological disorders, and Chief Scientific Advisor at SPR Therapeutics, which has developed a novel therapy for treating pain. In addition, he provides technical consulting to both small and large medical device companies. His research interests are in neural engineering and neuromodulation and include design and testing of electrodes and stimulation techniques, the electrical properties of tissues and cells, and computational neuroscience with applications to restoration of bladder function, treatment of movement disorders with deep brain stimulation, and electrical stimulation for treatment of pain. He has published over 170 peer reviewed journal articles and has been awarded 35 US patents.

Dr. Grill serves as a Consultant to the Neurological Devices Panel of the FDA Medical Devices Advisory Committee, a member of the Department of Veterans Affairs Secretary's Advisory Committee on Prosthetics and Special-Disabilities Program, and on the editorial boards of *Brain Stimulation, Journal of Neural Engineering*, and *Current Opinion in Biomedical Engineering*. He was elected as a Fellow of the American Institute of Medical and Biological Engineering in 2007, elected as a Fellow of the Biomedical Engineering Society in 2011, and was awarded a Javits Neuroscience Investigator Award by NIH-NINDS in 2015. Prof. Grill teaches courses on circuits and instrumentation, bioelectricity, and the fundamentals and applications of electrical stimulation. In 2008 he received the Capers & Marion McDonald Award for Excellence in Teaching and Research at Duke University, in 2013 was awarded Outstanding Postdoc Mentor at Duke University, and in 2014 received the University Scholar/Teacher of the Year Award at Duke.

Maysam Ghovanloo received the B.S. degree in electrical engineering from the University of Tehran, and the M.S. degree in biomedical engineering from the Amirkabir University of Technology, Tehran, Iran in 1997. He also received the M.S. and Ph.D. degrees in electrical engineering from the University of Michigan, Ann Arbor, in 2003 and 2004.

Dr. Ghovanloo developed the first modular Patient Care Monitoring System in Iran, where he also founded a startup to manufacture physiology and pharmacology research laboratory instruments. From 2004 to 2007 he was an Assistant Professor in the Department of ECE at the North Carolina State University, Raleigh, NC. Since 2007 he has been with the Georgia Institute of Technology, School of Electrical and Computer Engineering, where he is a Professor and the founding director of the GT-Bionics Lab. He has 8 issued patents and has authored or coauthored more than 200 peer-reviewed book chapters, conference, and journal publications on implantable microelectronic devices, integrated circuits and microsystems for medical applications, and modern assistive and rehabilitation technologies.

Dr. Ghovanloo is an Associate Editor of the *IEEE Transactions on Biomedical Engineering* and *IEEE Transactions on Biomedical Circuits and Systems*. He was a CAS Society Distinguished Lecturer in 2015–2016. He was the general chair of the *IEEE Biomedical Circuits and Systems* (BioCAS) in Atlanta, GA in 2015. He served as an Associate Editor of *IEEE Transactions on Circuits and Systems, Part II* from 2008–2011, as well as a Guest Editor for the *IEEE Journal of Solid-State Circuits* and *IEEE Transactions on Neural Systems and Rehabilitation Engineering*. He has also served on the Imagers, MEMS, Medical and Displays subcommittee of the *International Solid-State Circuits Conference* (ISSCC) from 2009–2014. He has received the National Science Foundation CAREER Award, the Tommy Nobis Barrier Breaker Award for Innovation, and Distinguished Young Scholar Award from the Association of Professors and Scholars of Iranian Heritage.

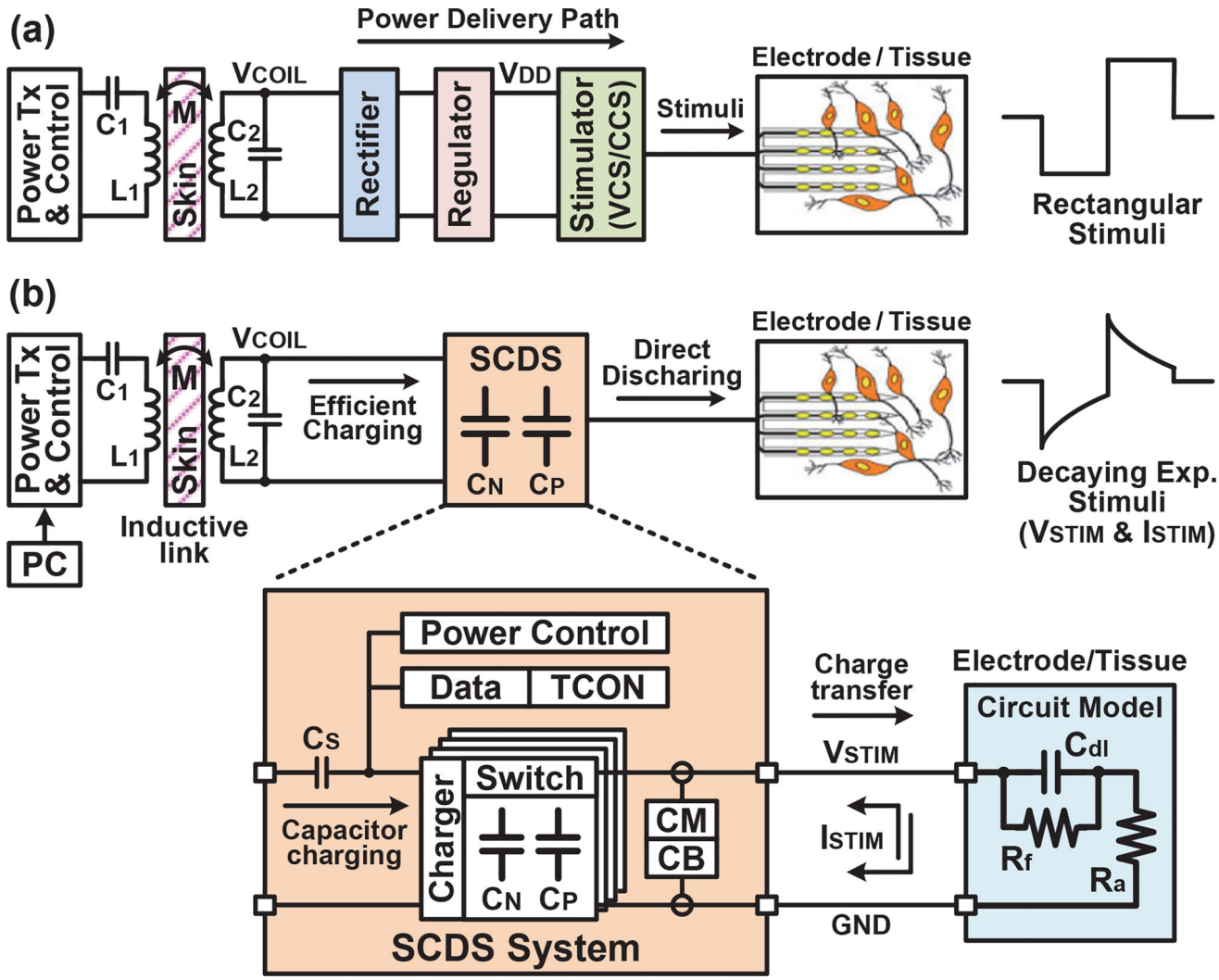

Fig. 1.

Key power delivery/management blocks and stimulus waveforms of wireless stimulation systems. A power transmitter (Tx) drives a primary coil, L_1, at the carrier frequency, f_C, generating an ac voltage, V_{COIL}, across a secondary coil, L_2. (a) A conventional wireless system with voltage-controlled stimulation (VCS) or current-controlled stimulation (CCS). A rectifier and a regulator convert V_{COIL} to dc output voltage, V_{DD}, to supply a stimulator, which typically generates rectangular voltage or current stimuli. (b) The proposed wireless system with switched-capacitor discharge stimulation (SCDS). The SCDS system efficiently charges a storage capacitor bank, C_N and C_P, directly from the inductive link and transfers charge from the capacitors to tissue, generating decaying exponential stimuli.

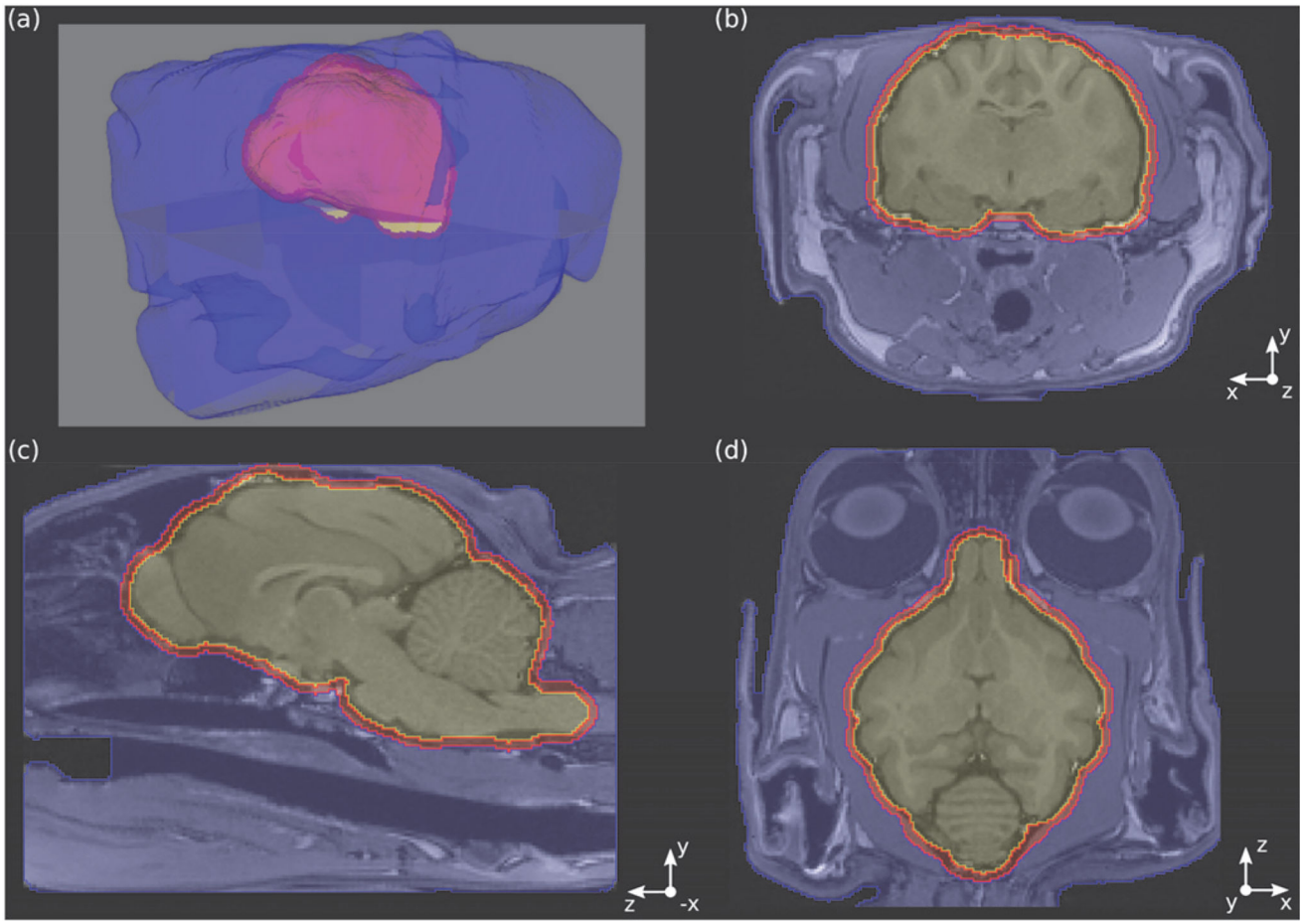

Fig. 2.

A magnetic resonance image of the cat head segmented into three regions. (a) A T1-weighted (T1w) magnetic resonance (MR) image was used to construct three volumes: a brain (*yellow*), a skull that surrounds the brain (*red*), and a region of lumped soft tissues (*blue*). Binary masks of the segmented volumes were overlaid on the T1w MR image and viewed in (b) coronal, (c) sagittal and (d) axial planes. The positive x axis points to the right of the head; the positive y direction in the superior direction (i.e., toward the top of the head); and, the positive z direction in the anterior direction (i.e., toward the mouth).

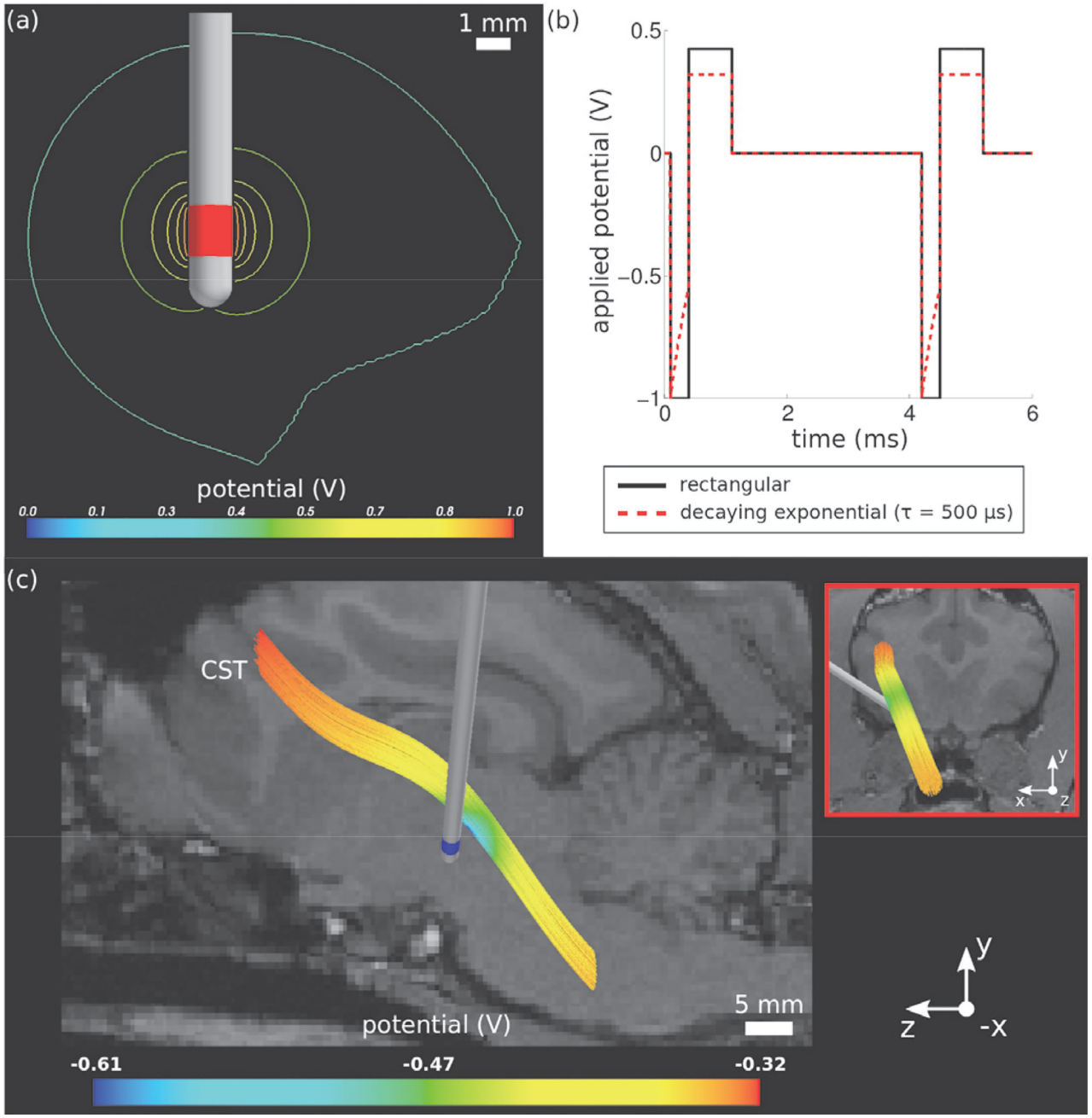

Fig. 3.

Electrical stimulation of corticospinal tract (CST) axons in a model of the cat head. (a) Isopotential contours surrounding the active electrode in monopolar anodic configuration. (b) Applied rectangular and decaying exponential waveforms were voltage-regulated, asymmetric, and constructed so that the integral of the waveform with respect to time was zero. Waveforms consisted of a short 300 μs cathodic phase followed by a long 700 μs anodic phase and were delivered at 244 Hz. Note: normalized waveforms are shown in this graph. (c) The spatiotemporal distribution of extracellular potentials formed from parts a and b, based on (3), was used to stimulate CST axons in the model. The image shows the

extracellular potentials applied to the CST axons at the onset of the stimulus pulse. Inset: a coronal view.

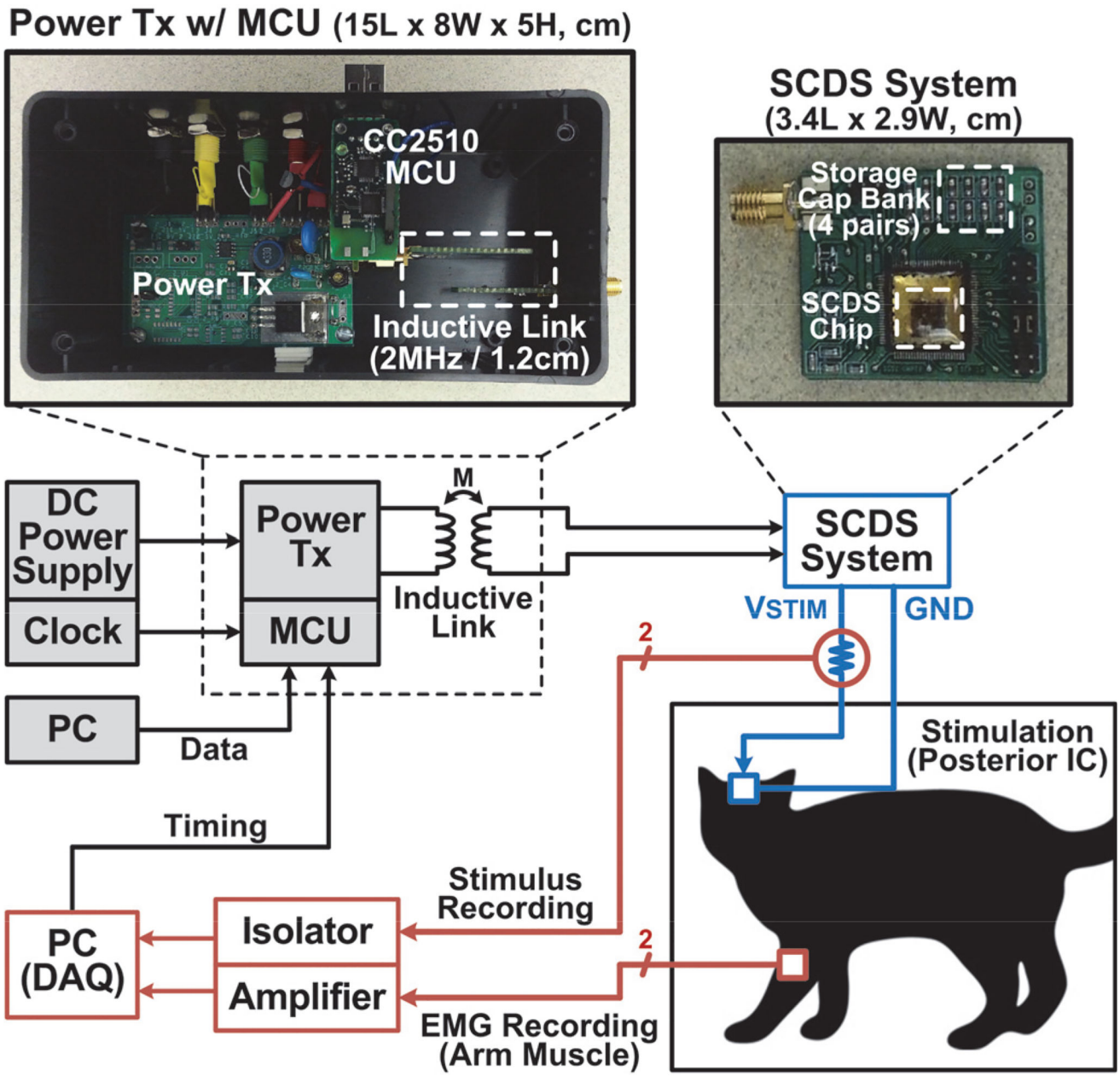

Fig. 4.

Block diagram of the *in vivo* experimental setup with the SCDS system. The wirelessly-powered SCDS system and its recording setup enable simultaneous brain stimulation to the posterior IC and EMG recording from the upper arm muscles, respectively. The power Tx module, including the 2 MHz inductive link with primary ($\varnothing_1$ = 2 cm) and secondary ($\varnothing_2$ = 1 cm) coils and 1.2 cm coil spacing, was enclosed in a 15 (L) × 8 (W) × 5 (H) cm^3 box. The SCDS prototype PCB occupied 3.4 × 2.9 cm^2 and housed the SCDS chip (5 × 2.4 mm^2), 4 pairs of off-chip storage capacitors (1.6 × 0.8 mm^2 each, 5–10% tolerance, X5R/X7R, capacitance of 1 μF, 1 μF, 3.3 μF, and 4.7 μF), and a few off-chip components for testing.

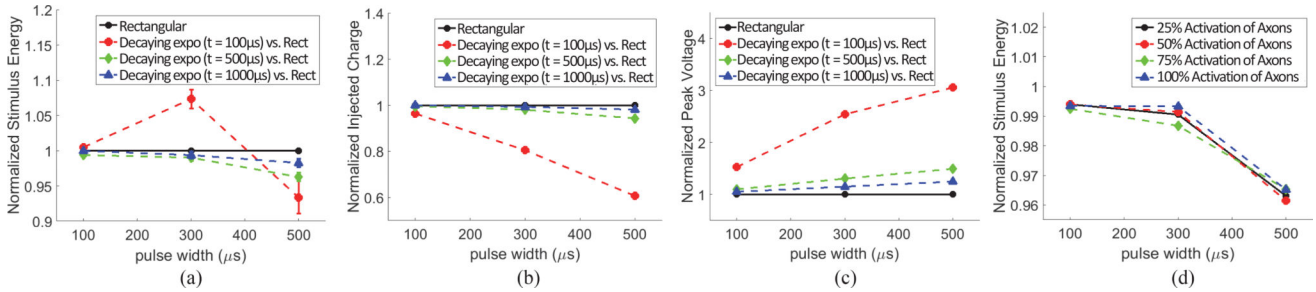

Fig. 5.

Efficiencies of rectangular and decaying exponential stimulus waveforms from computational models. Normalized (a) stimulus energy, (b) injected charge, and (c) peak stimulus voltage required to activate 50% of the population of model axons. Each result is the median value from 300 samples normalized by the value for the rectangular stimulus. (d) Normalized stimulus energy for decaying exponential waveforms with τ = 500 μs to activate 25%, 50%, 75%, and 100% of the population of model axons.

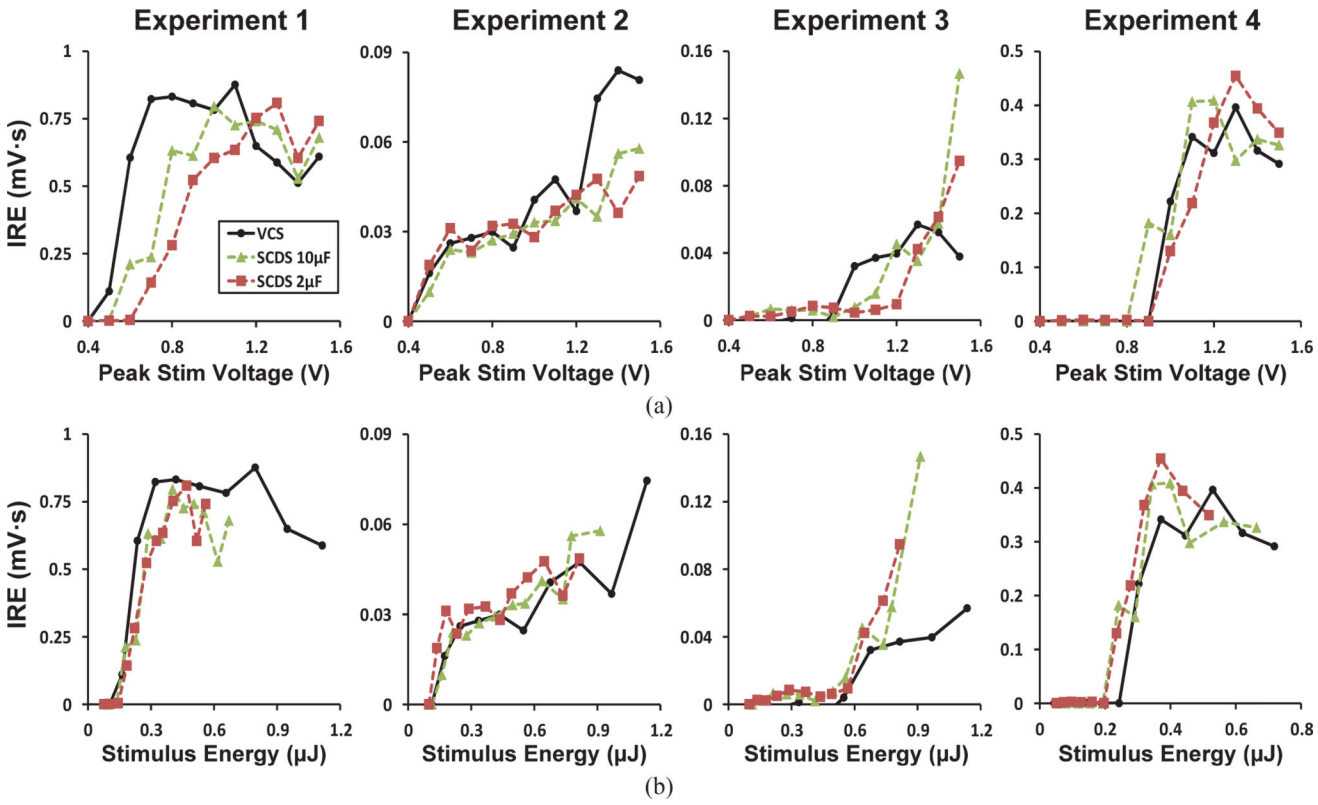

Fig. 6.

In vivo stimulation efficiency of the SCDS system compared to the conventional VCS system. (a) The integral of rectified EMG voltage (*IRE*) vs. peak stimulus voltage and (b) *IRE* vs. stimulus energy graphs from *in vivo* experiments ($n = 4$).

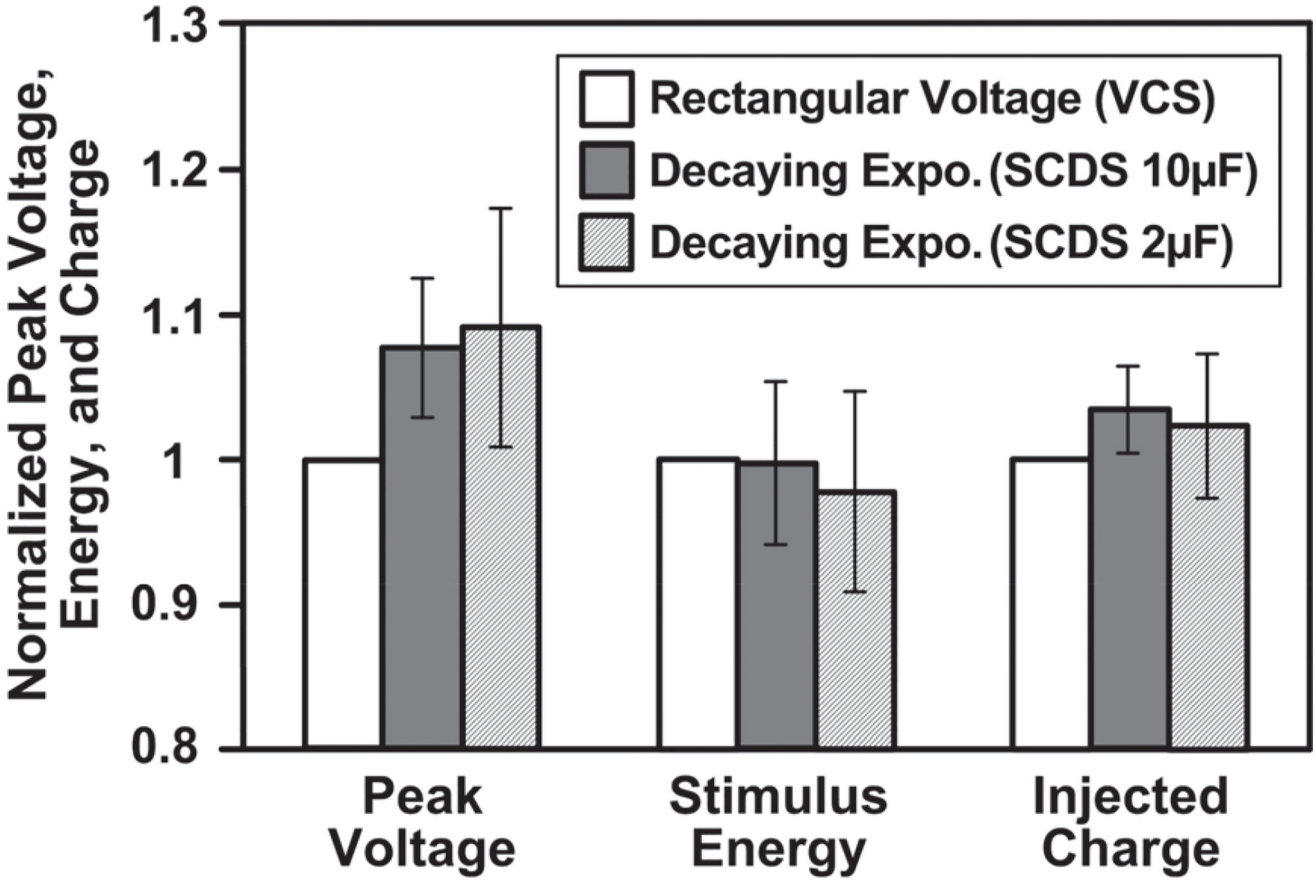

Fig. 7.

Comparison of stimulation efficiencies between SCDS and VCS systems. Peak voltage amplitude, stimulus energy, and injected charge of SCDS-based decaying exponential stimuli (storage capacitance of 2 μF or 10 μF) required to activate the half maximal *IRE*, normalized by those of VCS-based rectangular voltage stimuli (mean ± standard error, n = 4), based on (5).

Table I

Specifications of the Wireless SCDS System

Overall System		**Switched-capacitor stimulation**	
Technology	0.35 μm CMOS	# of channels	4 active + 4 return
Carrier freq.	2 MHz	Stim. freq.	7.6 – 244 Hz[A]
System supply	2.1 V / −2.1 V	Pulse width	16 – 512 μs[A]
Wireless capacitor charger		Current limiter	0.012 – 1.5mA[B]
Cap. voltage	±0.4 – ±2 V	Charge balancing	Charge monitor + passive
Storage cap.	1 – 4.7 μF		
Charging eff. / time	43 – 82% / 36 – 420 μs	Charge transfer eff.	95 – 98%

[A] 5-bit adjustable,

[B] Can be deactivated to allow higher peak currents.

Table II

Benchmarking Wireless IPG Systems

IPG Structure		**VCS**[A]	**Dynamic supply VCS + CCS [47]**	**CCS [57]**	**Dynamic voltage scaling CCS [58]**	**SCDS [26]**
Supply voltage (V)		±2.1	3.3	±12	6	**±2.1**
IPG system efficiency (%)	Rectifier[B]	80	80	80	80	-
	Regulator[C]	87.5	91.7	97.5	95.2	-
	Capacitor charger[D]	-	-	-	-	**43 ~ 82 (V_{CAP} = ±0.4V ~ ±2V)**
	Stimulator[D]	19 ~ 95.2 (V_{STIM} = ±0.4V ~ ±2V)	55 ~ 94 (V_{STIM} = 0.4V ~ 3V)	3.6 ~ 54.2 (I_{STIM} = 33μA ~ 500μA)	2.4 ~ 70 (I_{STIM} = 8μA ~ 504μA)	**95 ~ 98 (V_{STIM} = ±0.4V ~ ±2V)**
	Total	13.3 ~ 66.6	40.3 ~ 69	2.8 ~ 42.3	1.8 ~ 53.3	**40.9 ~ 80.4**
Stimulus shape		Rectangular voltage	Pseudo rectangular current	Rectangular current	Rectangular current	**Decaying expo. voltage**
Series *RC* model		0.5kΩ + 1μF	1kΩ + 0.93μF	10kΩ + 100nF	6.8kΩ + 6.9nF	**0.5kΩ + 1μF**
Relative stimulation energy ratio, f_{STIM}[E]		1	-	-	-	**0.98**
Overall energy saving ratio, *ESR*, compared to VCS (%)[E]		0	-	-	-	**40.7**
Injected charge control method		Hard to control injected charge	Adjust V_{STIM} by sensing stim. current	Adjust current amplitude & time	Adjust current amplitude & time	**Adjust capacitance & voltage level**

[A] Conventional VCS system calculated in Section II-E and III-C for system efficiency comparison with the SCDS system,

[B] Average efficiency is estimated in [43],

[C] Assumed small voltage drop of 0.3V with closed-loop supply control in [59],

[D] Estimated with measured results in references,

[E] Calculated with *in vivo* measured results in Section III-C